A NEW EVAPORATOR FOR THE LITHIUM DEPOSITION CHAMBER AT HOUGHTON UNIVERSITY

By

Asher Knight

A thesis submitted in partial fulfillment of the
requirements for the degree of

Bachelor of Science

Houghton University

May 2026

Signature of Author……..
Department of Physics
May 6, 2026

……
Dr. Mark Yuly
Professor of Physics
Research Supervisor

……
Dr. Brandon Hoffman
Professor of Physics

A NEW EVAPORATOR FOR THE LITHIUM DEPOSITION CHAMBER AT HOUGHTON UNIVERSITY

By

Asher Knight

Submitted to the Department of Physics
on May 6, 2026 in partial fulfillment of the
requirement for the degree of
Bachelor of Science

Abstract

Light ion nuclear reaction experiments using ultra-fast high-power lasers performed at the Lab for Laser Energetics (LLE) use thin lithium films to measure nuclear cross sections using Inertial Confinement Fusion (ICF) or Target Normal Sheath Acceleration (TNSA). To make these films, a new lithium evaporator system has been developed at Houghton University. The new evaporator is easier to install, separates the two evaporator boats in order to evaporate one material at time for multilayer targets, uses a linear feedthrough to position the substrates, and incorporates a deposition rate monitor to control the layer thickness. Because lithium reacts with air, the new design allows the creation of a protective layer to coat the lithium film, and the deposition chamber is inside of an argon glove box.

Thesis Supervisor: Dr. Mark Yuly
Title: Professor of Physics

TABLE OF CONTENTS

TABLE OF FIGURES

Chapter 1

INTRODUCTION TO THE LITHIUM DEPOSITION CHAMBER

1.1. Overview

Over the past ten years, a new detector system called the Short-Lived Isotope Counting System (SLICS) has been developed at Houghton University in collaboration with researchers from SUNY Geneseo in the Laboratory for Laser Energetics. The purpose of this detector is to carry out nuclear physics measurements involving light ions using Target Normal Sheath Acceleration (TNSA) and Inertial Confinement Fusion (ICF) [1].

As part of developing this diagnostic, many tests and benchmark experiments have been carried out. Because of its unique nuclear and mechanical properties, thin lithium films were used as targets for these measurements. This thesis describes the development of the physical vapor deposition system used to create these thin lithium targets.

1.2. Motivation

The development of the SLICS detector and experiments using it required precise nuclear targets, on the scale of micrometers thick. Specifically, thin lithium films must be made with controlled thickness and uniformity to ensure accurate measurements. Because the performance of both TNSA and ICF experiments depends strongly on the specifications of the target material, it is essential to understand the physics behind these experiments

1.2.1. Target Normal Sheath Acceleration (TNSA)

TNSA, as seen in Figure 1, is a process in which a high-intensity laser pulse can accelerate ions off the surface of a target. A laser pre-pulse first creates a plasma, so that when the main laser pulse strikes the electrons are blown through the target and out the other side, creating a strong magnetic field that accelerates the positively charged ions away from the surface of the target. The accelerated ions can then strike a secondary thin-film nuclear target placed behind the first. Nuclear reactions that occur in the nuclear target can lead to radioactive product nuclei, which beta decay much later. The beta particles can then be detected by the

SLICS detector. This method generates high-energy ion beams without the use of traditional accelerators [1].

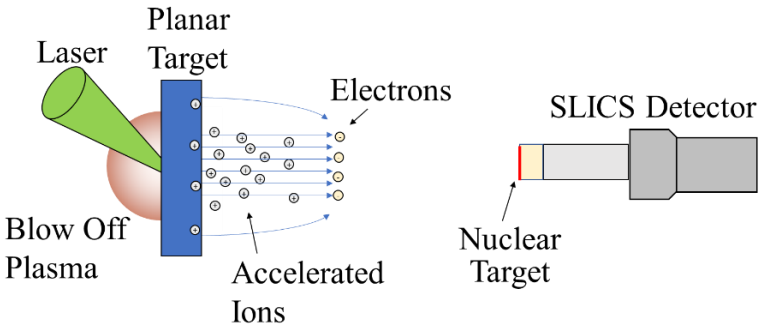

Figure 1. Target normal sheath acceleration (TNSA). An intense laser pulse strikes a solid target, generating a sheath field that accelerates ions away from the surface, which then travel outward and collide with a nearby nuclear target

1.2.2. Inertial Confinement Fusion (ICF)

Figure 2 shows the second technique, ICF, in which lasers are used to compress and heat a target containing nuclear fuel, such as deuterium or tritium, to very high temperatures and pressures.

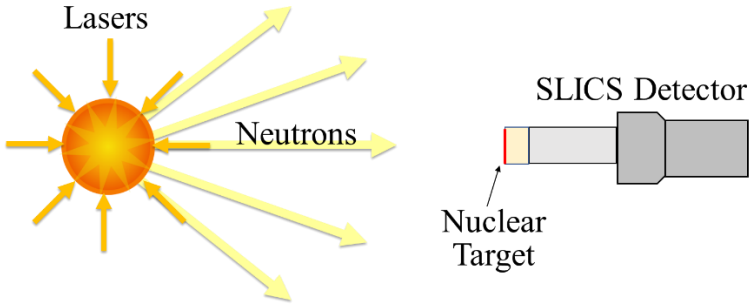

Figure 2. Neutron induced reactions. High-powered lasers compress and heat a fuel capsule to initiate fusion reactions, producing a burst of energetic neutrons that escape the capsule and strike a surrounding nuclear target.

When the lasers hit the capsule the outer layer is heated rapidly and ablates. This causes an inward force that compresses and heats the deuterium or tritium, forming a plasma and causing nuclear reactions to occur at the center. This produces a burst of energetic neutrons

which interact with surrounding materials. A nuclear target can be placed in front of SLICS so that these neutrons will collide with it and cause reactions which can be detected with the detector [1].

Figure 3 shows another type of ICF reaction which occurs when a doped nuclear target is used for the initial compression. In this model the target is still compressed using high-powered lasers; however, the desired thermonuclear reactions occur between ions in the ICF hot spot, as opposed to neutrons striking a subsequent target. The product nuclei in the compressed target then burst out in all directions. A detector with a getter foil is placed so that the product nuclei hit and stick to the getter foil, where they can slowly beta decay, which the SLICS detects.

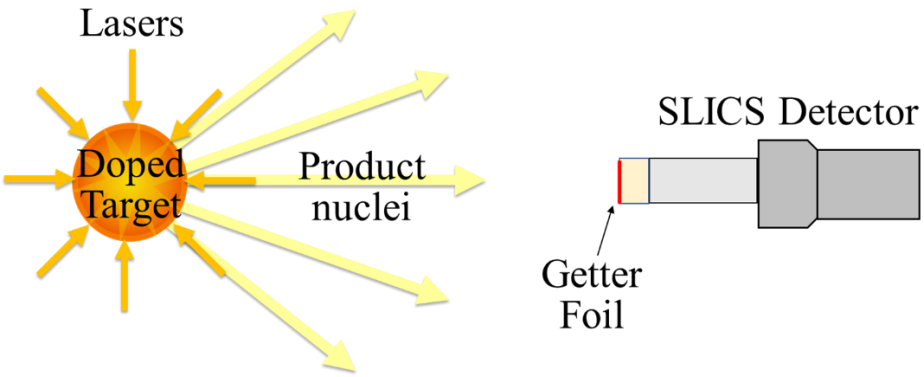

Figure 3. Inertial confinement fusion using a doped nuclear target. As the target is compressed, nuclear reactions occur. The product nuclei explode out and hit a getter foil, where they remain as they beta decay into the detector.

1.2.3. Lab for Laser Energetics

These experiments are carried out at the Laboratory for Laser Energetics (LLE) in Rochester, which houses high-powered laser systems capable of performing both TNSA and ICF experiments. The facility provides the necessary infrastructure to generate intense laser pulses, using lasers such as the Multi-Terawatt Laser (MTW), OMEGA, and OMEGA EP lasers. The Houghton University physics department has collaborated with them on several experiments.

1.2.4. Short-Lived Isotope Counting System (SLICS)

These types of ICF and TNSA experiments are made possible by the unique characteristics of the SLICS detector, which, rather than detecting the prompt radiation from the reaction, counts the decays of the product nuclei in the quiet environment long after the laser shot. As unstable product nuclei on the getter foil or in the nuclear target decay, their emitted particles pass through two scintillators which convert energy lost into light pulses. The light signals are transmitted through a light guide to a photomultiplier tube, which converts light to an electrical signal. These signals are recorded for later analysis. By measuring decay counts, SLICS enables cross section measurements for short-lived isotopes that would be difficult to study with conventional methods.

1.2.5. Previous Experiments

As the SLICS detector was being developed, a number of tests were carried out that required thin lithium films. One of the first was the "exploding wire" experiment, shown in Figure 4.

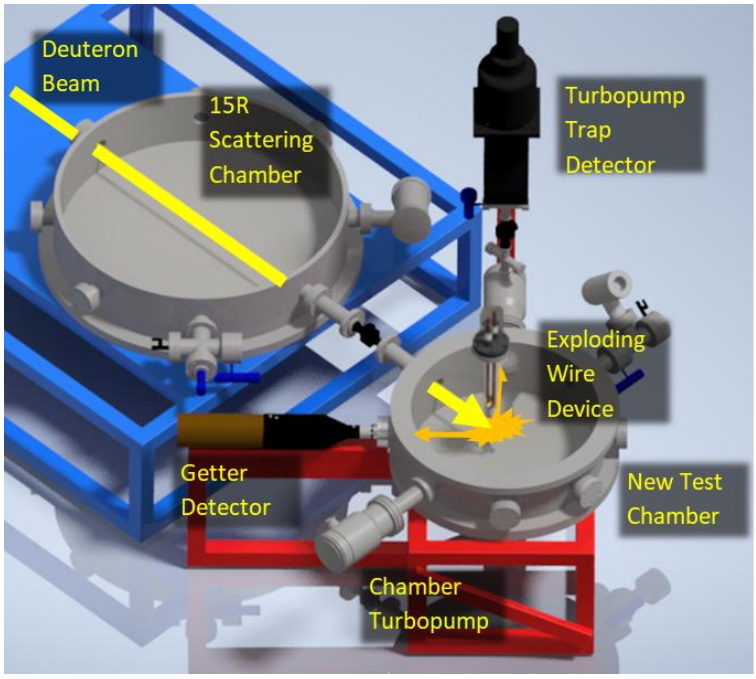

Figure 4. The "exploding wire" experimental setup. A beam of deuterons was shot at a tungsten ribbon coated in lithium. Approximately 1000 amps were sent through the ribbon and the lithium was vaporized and flew out in all directions, striking the SLICS detector, where it beta decayed. Figure taken from Ref [2].

Carried out in 2022, this experiment was designed to simulate the plasma produced during ICF by vaporizing the copper off a copper-plated tungsten foil [2]. In this setup, a large electrical current was driven through the foil, causing intense heating that led to the rapid vaporization of the copper. The resulting expanding cloud of hot material behaved like the neutral gas found after the recombination of the ICF plasma. This provided a controlled environment for a test of the SLICS detector to be performed.

In 2023 another experiment using thin target films was the Multi Terra-Watt (MTW) laser experiment, performed at LLE. Figure 5 shows the setup for this experiment, which involved the use of TNSA in which an intense, short-pulse laser was directed onto a deuterated target to accelerate deuterons to MeV energies. These ions were then directed onto a thin lithium target where ^{7}Li(d,p)^{8}Li nuclear reactions occurred. The resulting ^{8}Li nuclei beta decayed and were detected using the SLICS detector [1].

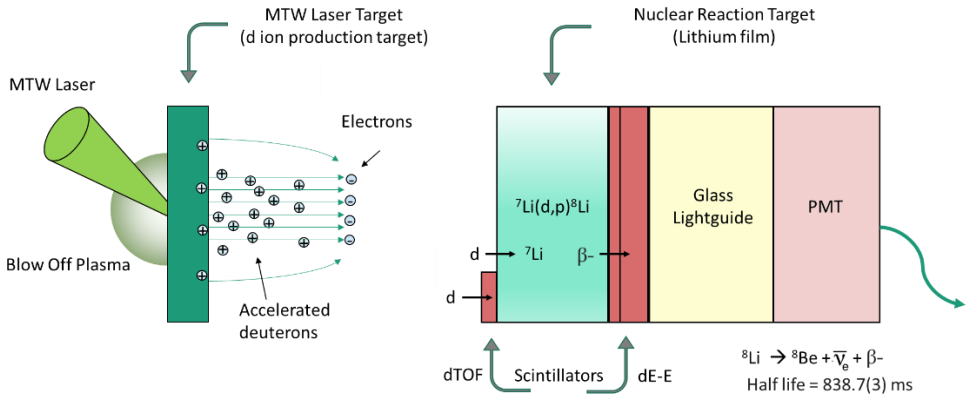

Figure 5. The 2023 MTW laser experiment setup. A laser prepulse struck a planar target, creating a plasma. The main laser then struck the target, causing electrons to travel through and create an electric field, pulling off deuterons. These deuterons struck a thin lithium film and caused nuclear reactions which beta decayed into the detector. Figure taken from Ref [1]

An experiment in 2024 measured the absolute efficiency of the SLICS detector by directly comparing the number of ^{8}Li isotopes produced by ^{7}Li(d,p)^{8}Li to the number of decays actually detected. Deuterons from the SUNY Geneseo pelletron accelerator struck a thin lithium target, producing ^{8}Li, and the resulting decays were counted with SLICS as seen in Figure 6 [3].

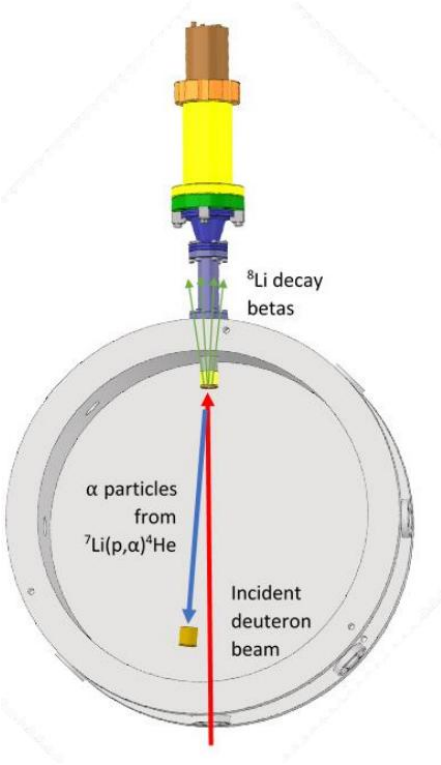

Figure 6. The 2024 SLICS beta detection efficiency experimental setup. A deuteron beam from the pelletron accelerator struck a thin lithium target causing nuclear reactions, the ^{8}Li products of which beta decayed into the SLICS detector. Taken from Ref [3].

In 2025 the OMEGA-EP laser facility at LLE was used to perform a TNSA experiment. This experiment, shown in Figure 7, used thin lithium films as nuclear targets in the TNSA process [4]. The experiment measured the production of ^{8}Li through the ^{7}Li(d,p)^{8}Li reaction. It showed that TNSA ions can induce nuclear reactions that produce radioactive products that can be detected using SLICS. It also showed how lithium films degrade after being used in a shot.

1.3. Overview of Project

From the preceding explanation, it is hopefully evident why the capability to produce thin target films was needed. A deposition chamber enables the creation of thin films on substrates in a vacuum. These films, with thicknesses ranging from nanometers to micrometers, are particularly useful as targets for nuclear physics experiments because they minimize energy loss before and after nuclear reactions with incoming particles.

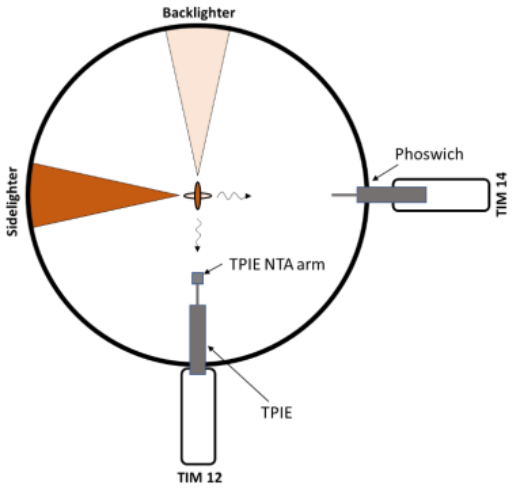

Figure 7. The setup for the 2025 OMEGA-EP experiment. A backlighter laser accelerates deuterons towards the Thomson Parabola Ion Energy (TPIE) detector, while a sidelighter laser strikes the laser target to produce deuterons that strike the thin lithum film on the end of the phoswitch detector. Figure taken from Ref [4].

In the Houghton system, the deposition chamber is connected to vacuum pumps to evacuate the chamber, creating a low-pressure environment that minimizes contamination, allows particles to travel freely and provides a base pressure much below the vapor pressure of the desired evaporant. Inside the chamber, an evaporator is used to heat the evaporant material until it vaporizes, forming a stream of atoms, as seen in Figure 8. These atoms then travel through the vacuum and deposit onto a cool substrate, which is held in place by a substrate holder.

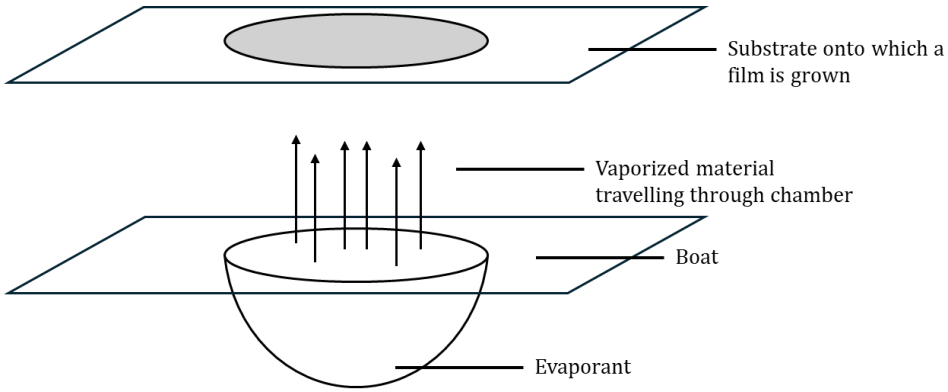

Figure 8. The deposition process. The evaporant substance in the boat is heated up until it vaporizes. Atoms of evaporant then travel accross the chamber to the substrate where they are deposited.

The process of creating thin films using evaporation is called Physical Vapor Deposition (PVD). In this process, materials are vaporized by an energy input, such as thermal heating, electron beam bombardment, or sputtering (the vaporization of a target material via high-energy ion bombardment). The now-evaporated atoms travel towards a substrate, gradually forming a thin metal film as they are deposited [1].

Physical vapor deposition has its origins in the study of vacuum physics conducted in the late 19th and early 20th centuries. Researchers such as Irving Langmuir [5] observed that vaporized metals could be deposited as thin films onto substrates. As vacuum pumps and seals improved throughout the 20th century experimentation with PVD improved. Langmuir's work with sputtering (the vaporization of a target material via high-energy ion bombardment and the subsequent deposition of those atoms on a substrate) marked a significant improvement in PVD techniques. Sputtering represents a specific technique within physical vapor deposition, which uses ion bombardment to remove material from a target rather than relying on thermal evaporation, which is the method used at Houghton University. Thermal evaporation was studied by R. von Pohl and P. Pringsheim, who demonstrated the first practical application of thermal evaporation by evaporating silver onto glass [6].

Vacuum chambers have been critical in the development of PVD techniques. Early vacuum chambers were used to study gas pressure [7], atmospheric phenomena [8], and the behavior of gases under low pressure [9], with subsequent chambers being designed with the goal of reducing contamination during evaporation experiments [5]. Throughout the 20th century, advances in vacuum technology improved sealing, pumping efficiency, and pressure measurement, enabling high and ultra-high vacuum conditions [10]. These low-pressure environments are essential for PVD, as they reduce contamination and increase the mean free path of atoms, allowing them to travel ballistically from the source to the substrate. As a result, modern vacuum chambers provide the controlled conditions necessary for thin film deposition.

In 2022, the first prototype deposition system was constructed at Houghton University [11]. The deposition system has gone through several design iterations. The new design, the

subject of this thesis, improves both usability and experimental control. Attaching the evaporator at the bottom simplifies insertion and removal, especially with the O-ring seal. A divider separates the two evaporating boats, reducing the risk of cross-contamination, and the movable substrate holder can block the openings to further prevent mixing. This design also makes substrate insertion easier and includes a rate monitor for better control of deposition. Also, the substrate is cooled through heat transfer along a linear feedthrough, and a repositioned viewport provides improved visibility during operation.

1.4. Existing Evaporator System

To better understand these improvements, it is useful to first examine the existing evaporator system. The existing design for the evaporator system is built off two copper rods, attached to a copper feedthrough. The copper feedthrough maintains the vacuum seal while still allowing current to travel into the chamber from an outside power source. These copper rods carry current through two “boats”, which hold the desired target material and heat up and evaporate the material. This causes the material to leave the boat as it travels towards the substrate.

The boats are electrically attached to the copper rods via two diodes as seen in Figure 9. The diodes allow the heating of only one boat at a time, which is crucial for the creation of multilayer targets, as a different material can be placed in each boat and deposited one after another, layering a second deposition on top of the first. Multilayer targets allow researchers to study nuclear reactions between specific material combinations or add a layer of protective material to prevent the desired target material from becoming contaminated. The evaporator includes a house, which is a thin steel covering that has holes on top to allow evaporated material to travel towards the substrate, which rests above.

The evaporator system and feedthrough are inserted into the deposition chamber through a flange. This port is rotatable, which means care is required in order to ensure that the boats are level inside of the chamber, as this is not guaranteed. Additionally, it is difficult to insert the evaporator without bumping the diodes on the side of the chamber. Electrical contact with the chamber must be avoided, as it can disrupt operation and damage equipment. Because the chamber is conductive, any contact creates a low-resistance path to ground,

causing the current to bypass the evaporator boats. This diverts current away from the intended heating path, preventing proper evaporation and potentially overloading or damaging the power supply.

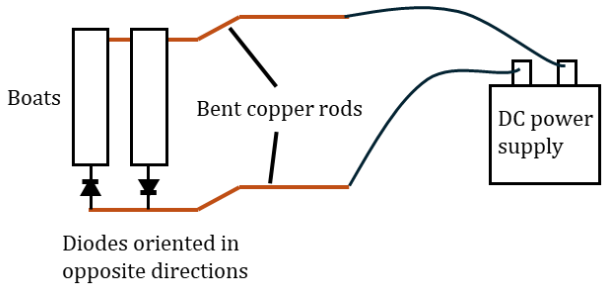

Figure 9. A simplified schematic of the evaporator. The diodes prevent both boats from heating simultaneously; when current flows clockwise, the leftmost boat is heated and when current flows counterclockwise the rightmost boat is heated. The copper rods are electrically connected to a DC power supply.

1.5. Description of Proposed Changes

While the current evaporator in the Houghton University deposition chamber effectively does its intended task, it has limitations. The evaporator is inserted via a port on the side of the chamber, making it both difficult to maneuver and install, as it is wide and the copper rods are bent downward so the evaporator tends to bump the sides during installation. The vacuum seal required a large O-ring which is challenging to keep in place during installation. In addition, the current design relies on ceramic screws in its assembly, which are brittle and prone to breaking during handling. Also, the current design has issues with cross-contamination between different materials and offers limited visibility of the evaporation process. The system also doesn't give us information about the film as it is being made, other than temperatures of the boats and the house.

The proposed changes to the lithium deposition system will improve both the precision and usability of the evaporator system. The new design moves the evaporator port to the bottom of the chamber, simplifying installation and making it easier to maintain an O-ring seal. The updated configuration reduces the risk of the assembly contacting the chamber walls during insertion, includes a divider between the boats, and has a movable substrate, which allows for better control over deposition.

The new design includes an optional deposition rate monitor which can be inserted from the top. A deposition rate monitor is used to measure the thickness and deposition rate of thin films as they are formed. Additionally, a viewport is being placed for improved observation of the evaporation process, and attaching the substrate holder to a linear feedthrough will allow for better thermal management of the substrate.

Chapter 2

THEORY OF VAPOR DEPOSITION

In order to reliably produce thin film targets it is necessary to understand the physical principles that affect thin film deposition, including mean free path, vapor pressure, and evaporation flux. These factors affect the thickness and evenness of the lithium films produced by vapor deposition.

2.1. Vacuum Chamber Theory

2.1.1. Purpose of Vacuum Chamber

Vacuum chambers are essential for vapor deposition because they reduce background molecules that can react with the evaporant, scatter vaporized atoms, contaminate the deposited film, and keep it from evaporating. Maintaining a controlled vacuum environment ensures consistent deposition rates and high-purity thin films. Vacuum conditions also increase the mean free path of evaporated particles, allowing them to travel directly from the target to the substrate without interruption from other gas molecules. This low-pressure environment also improves evaporation because reducing pressure increases the rate of which atoms leave the surface, allowing materials with enough vapor pressure to evaporate easily.

In thermal evaporation, desired film material is placed in a boat and heated until it vaporizes, as seen in Figure 10. The internal energy of atoms in the material increases until they evaporate off the surface and travel through the chamber to the substrate. If the pressure is too high in the chamber then these atoms will likely hit background gas molecules. For lithium specifically it is crucial that the chamber has minimal background gas molecules, as lithium readily reacts with air.

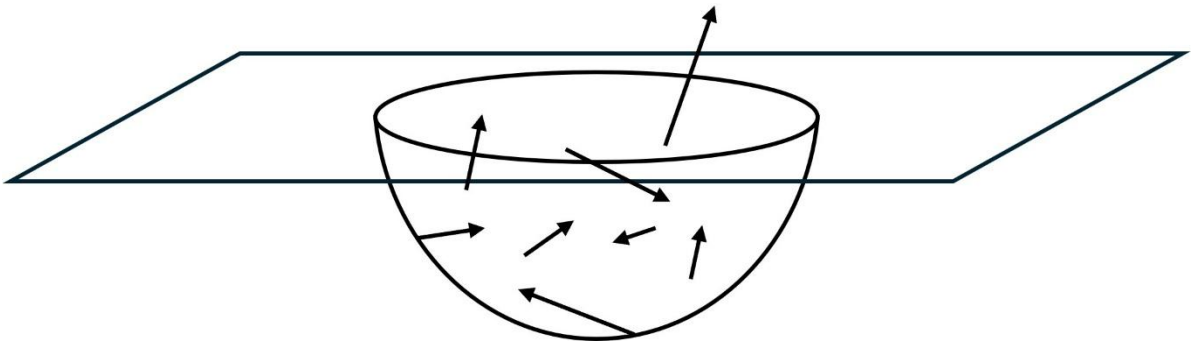

Figure 10. Boat with evaporant material filling in a divot. As current goes through the boat the atoms of the material are heated until their internal energy causes them to break free from the surface.

2.1.2. Pressure and Gas in the Chamber

The behavior of the residual air molecules in the chamber can be described using the ideal gas law

$$PV = n_{moles}RT, \tag{1}$$

where P is the pressure, V is the volume of the chamber, n_{moles} is the number of moles of residual gas, R is the gas constant 8.314 J mol^{-1} K^{-1}, and T is absolute temperature. By lowering the pressure in the chamber the gas density is lowered to a degree with which vaporized atoms can freely travel to the substrate without colliding with air molecules.

2.1.3. Mean Free Path

In other words, lowering pressure inside of the chamber increases the mean free path of gas molecules. Mean free path (λ) is the average distance an atom travels between collisions with other particles. Following Ref [12] the mean free path can be derived as follows.

Consider a molecule moving through gas with n molecules per unit volume. Each molecule has an effective collision cross section σ, which represents the area it presents for collisions. As the molecule travels a distance L it sweeps out the cylindrical volume

$$V = \sigma L. \tag{2}$$

The expected number of collisions (N) the molecule will have as it travels is therefore

$$N = n_{density}\sigma L\,, \tag{3}$$

where $n_{density}$ is the number density of particles in the gas. The mean free path (λ) is the distance a particle travels on average before one collision occurs. This means that $N = 1$ when $L = \lambda$. Using this, Equation (3) becomes

$$1 = n_{density}\sigma\lambda\,, \tag{4}$$

which, when solved for λ, becomes

$$\lambda = \frac{1}{n_{density}\sigma}\,. \tag{5}$$

However, in reality all molecules in the gas are moving, which must be accounted for. The collisions depend on how fast they approach each other (relative velocity):

$$\vec{v}_{rel} = \vec{v}_1 - \vec{v}_2 \tag{6}$$

The molecules do not all have the same speed; instead, their velocities follow a thermal distribution. To account for this, consider the mean square relative speed, since collision rates depend on averages over the distribution. Taking the average of the square gives:

$$\langle {v_{rel}}^2 \rangle = \langle (\vec{v}_1 - \vec{v}_2) \cdot (\vec{v}_1 - \vec{v}_2) \rangle\,. \tag{7}$$

Expanding gives

$$\langle {v_{rel}}^2 \rangle = \langle {v_1}^2 \rangle + \langle {v_2}^2 \rangle - 2\langle \vec{v}_1 \cdot \vec{v}_2 \rangle\,. \tag{8}$$

For a gas in thermal equilibrium, both molecules are sampled from the same distribution, so

$$\langle {v_1}^2 \rangle = \langle {v_2}^2 \rangle = \langle v^2 \rangle\,, \tag{9}$$

and their velocities are randomly oriented, so there is no preferred direction in the gas. This means the average projection of one velocity onto another is zero:

$$\langle \vec{v}_1 \cdot \vec{v}_2 \rangle = 0. \tag{10}$$

Thus, Equation (8) becomes

$$\langle {v_{rel}}^2 \rangle = 2\langle v^2 \rangle \,, \tag{11}$$

or

$$v_{rel} = \sqrt{2}v. \tag{12}$$

Since collision frequency is proportional to relative speed, and mean free path is inversely proportional to collision frequency, the increase in relative speed by a factor of $\sqrt{2}$ reduces the mean free path by the same factor, giving

$$\lambda = \frac{1}{\sqrt{2} n_{density} \sigma} \,. \tag{13}$$

Now to solve for mean free path, Equation (1) can be rearranged for n_{moles}/V:

$$\frac{n_{moles}}{V} = \frac{P}{RT}, \tag{14}$$

where n_{moles} and $n_{density}$ are related by

$$n_{density} = \frac{N_A n_{moles}}{V}, \tag{15}$$

giving:

$$n_{density} = \frac{N_A P}{RT}, \tag{16}$$

where N_A is Avogadro's number. This can be used in Equation (13), giving

$$\lambda = \frac{1}{\sqrt{2}\sigma \left(\frac{N_A P}{RT}\right)}, \tag{17}$$

which simplified becomes

$$\lambda = \frac{RT}{\sqrt{2}N_A \sigma P}. \tag{18}$$

This demonstrates how mean free path is inversely proportional to pressure and further reinforces the need for vacuum conditions during PVD. By reducing the pressure the mean free path is increased, meaning evaporated atoms can travel further with minimal collisions.

2.2. Physical Vapor Deposition (PVD) Theory

The process of PVD involves three steps: vaporization of materials, transport of atoms through a vacuum chamber, and condensation on substrate.

2.2.1. Thermal Evaporation

Thermal evaporation involves heating up a material, in the case of the Houghton University evaporator, by passing current through resistive boats. The evaporation rate can be found using the Hertz-Knudsen equation

$$J = \alpha \frac{P^* - P}{\sqrt{2\pi m k_B T}}, \tag{16}$$

where J is the evaporation flux (the atoms leaving the evaporator per unit area per second) α is the evaporation coefficient, which represents the fraction of atoms at the surface which actually evaporate, m is atomic mass of a single evaporating particle, k_B is the Boltzmann constant, P^* is vapor pressure (the pressure exerted by evaporated atoms) and P is ambient pressure. If $P \ll P^*$, $P \cong 0$, so following becomes true:

$$J \propto P^*, \tag{17}$$

which further reinforces the need for a vacuum to maximize evaporation [13]. When P is not much less than P^* there are more collisions with ambient gas molecules and evaporated atoms no longer evaporate and travel in straight paths to the substrate. Because the evaporation rate relates directly to the vapor pressure of the material, it is useful to examine vapor pressure curves, which show how vapor pressure changes with temperature for different materials. Specifically, a material must have a sufficiently high vapor pressure so

that atoms are emitted at a rate that causes thin film formation at the desired temperature. In order to ensure a long mean free path, the pressure in the deposition chamber must be very low.

Vapor pressure curves, such as those shown in Figure 11, show how equilibrium vapor pressure changes with temperature. The equilibrium vapor pressure is defined as the pressure at which the rate of atoms leaving the surface equals the rate returning to it. As temperature increases, the average kinetic energy of atoms increases, allowing a greater fraction of atoms to overcome the binding energy of the surface. This leads to a rapid increase in vapor pressure with temperature.

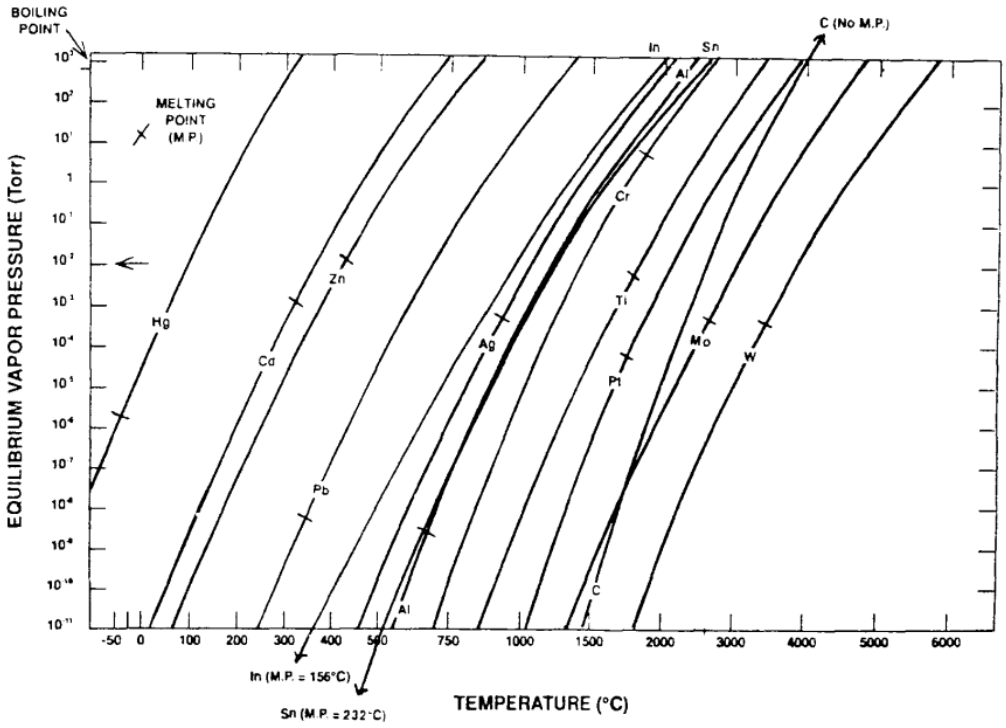

Figure 11. The vapor pressure curves for several selected materials. Each curve shows that vapor pressure increases rapidly with temperature, while the large separation between curves indicates that different materials require very different temperatures to reach the same vapor pressure. The marked melting points show where phase changes occur. Taken from Ref [12].

In thermal evaporation PVD, the vapor pressure determines the rate at which atoms leave the evaporant material. A sufficient vapor pressure is required for a reasonable deposition rate at a given temperature. Figure 12 shows that lithium reaches vapor pressures on the

order of 10^{-2} Torr at temperatures between 700 K to 900 K; however, the deposition system operates at 673 K, where lithium still has a nonzero vapor pressure sufficient for evaporation, but at a reduced deposition rate.

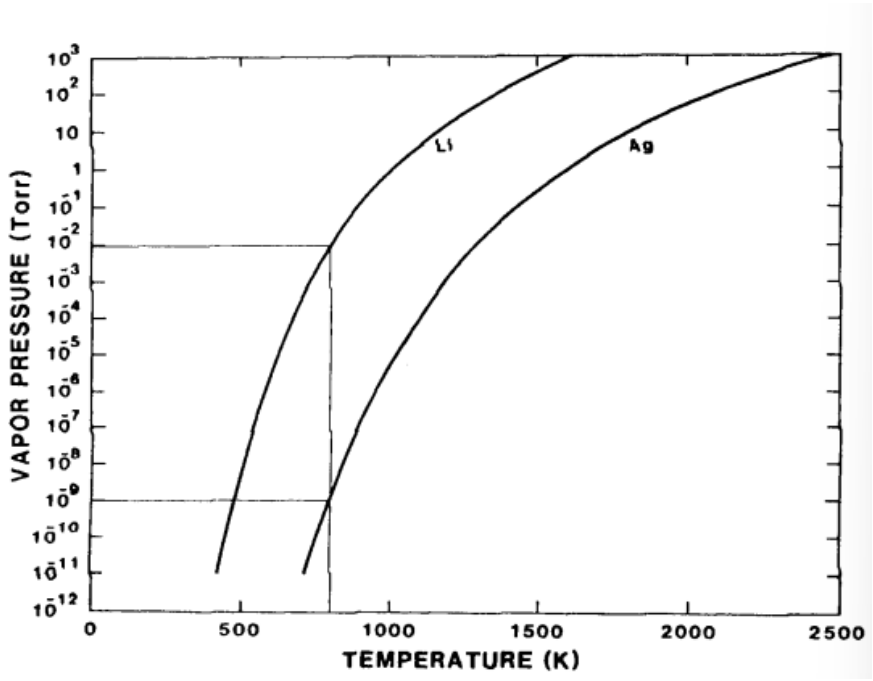

Figure 12. The vapor pressure curves for lithium and silver. The Houghton University deposition chamber operates at 673 K, which provides suitable vapor pressure for lithium evaporation. Taken from Ref [12].

The vapor pressure is different than the ambient chamber pressure. A sufficiently high vapor pressure is required to achieve an adequate evaporation flux from the source, while the chamber pressure must be lower (in the range of (10^{-5} to 10^{-6} Torr) to ensure stable vacuum conditions and prevent reduced evaporation at the source.

2.2.2. Transport to Substrate

In vacuum conditions the mean free path is very large, and atoms are free to travel ballistically from the evaporator to the substrate with minimal scattering. This results in a predictable deposition flux, allowing the film thickness to be directly related to the amount of material evaporated.

2.2.3. Condensation

The final step in the PVD process is condensation. When the vaporized atoms arrive on the substrate they go into a growing film. This is not the case for all evaporated atoms as they can also be reflected or re-evaporated. The probability of condensing depends on the temperature of the substrate and the energy in the arriving atoms. Higher substrate temperatures increase the probability of re-evaporating upon contact.

As the atoms arrive and condense, they release energy. This energy originates mainly from the heat of vaporization, kinetic energy, and chemical energy from any reactions at the substrate. This released energy influences film growth and structure by allowing the atoms to rearrange into more dense and ordered configurations.

2.2.4. Mass Distribution of Evaporated Material

In thermal evaporation the target material in the boat is heated. As it heats and atoms are evaporated off the surface (Figure 13), they leave with a velocity $\vec{v}$, and due to the mean free path they are able to travel in a straight line to the substrate.

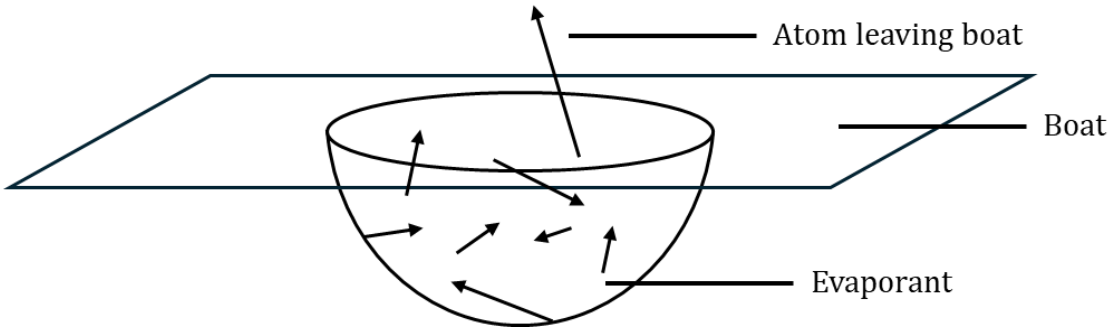

Figure 13. As the boat heats up the evaporant atoms begin to move quicker. Eventually their energy is enough that they break free from the surface and vaporize.

To derive an equation for the mass distribution of the deposited material the evaporating surface (boat) and condensing surface (substrate) must be considered separately, where dA_e is an infinitesimal area element on the evaporating surface and dA_c an infinitesimal area element on the susbtrate. Atoms evaporated from dA_e travel in every direction. To determine the number of atoms which travel towards the substrate we consider only those

moving within a small angle in the given direction. Over a short time dt, atoms with speed $\vec{v}$ travel a distance $\vec{v}dt$. The volume dV , shown in Figure 14, contains all of the atoms that reach dA_e in time dt:

$$dV = vdtdA_e. \tag{9}$$

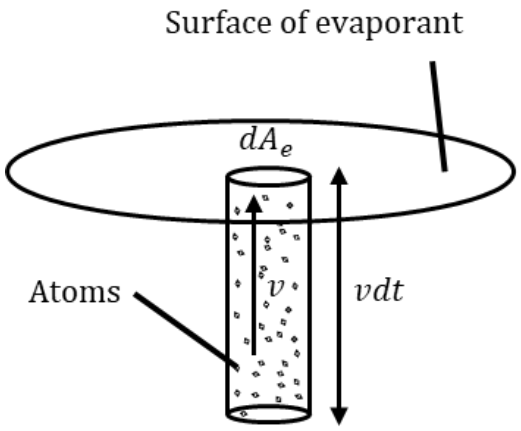

Figure 14. Volume element dV, defined by evaporant molecules leaving surface element dA_e with velocity $\vec{v}$ over a time interval dt. All atoms within this volume cross dA_e during this time interval.

However, Figure 15 shows what happens when the atoms do not leave the surface at a perfect vertical.

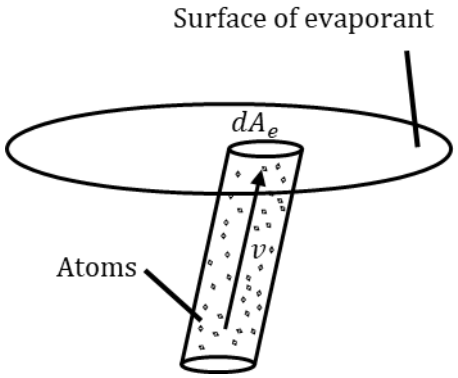

Figure 15. Volume element dV is angled when velocity $\vec{v}$ is not vertical.

Atoms are emitted at an angle ϕ relative to the normal of the surface. As shown in Figure 16, the same set of atoms crossing the surface element dA_e also crosses its projected area dA'_e. Since

$$dA'_e = dA_e \cos\phi\,, \tag{9}$$

the angular dependence is accounted for through the projected surface area rather than by considering only the normal component of velocity.

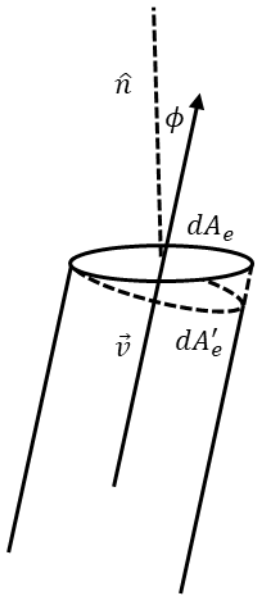

Figure 16. Geometric relation between the surface element dA_e and its projection dA'_e, used in determining swept volume dV.

Thus, dV becomes

$$dV = vdtdA_e \cos\phi\,. \tag{9}$$

Only a fraction of the evaporated atoms follow trajectories that intersect the condensing surface and subsequently stick to it, as seen in Figure 17.

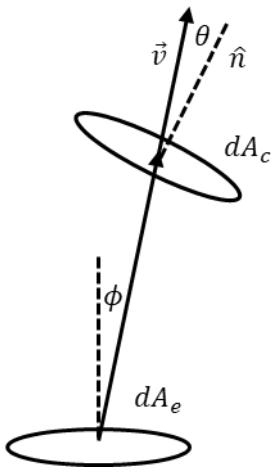

Figure 17. Atoms travel from the evaporating surface element dA_e to the condensing surface element dA_c in a straight line. Velocity $\vec{v}$ is at an angle ϕ normal to dA_e and at an angle θ normal to dA_c.

Atoms travel from the evaporating surface element dA_e to the condensing surface element dA_c in a straight line at velocity $\vec{v}$. To determine how many evaporated atoms reach the condensing surface, the solid angle can be considered. The solid angle ω is defined as the area subtended on a sphere divided by the square of the distance from the source. The effective condensing area of the surface element depends on its orientation relative to the incoming atoms. Only the component normal to the condensing surface needs to be considered, so a factor of $\cos\theta$ is introduced, making the differential solid angle

$$d\omega = \frac{dA_c \cos\theta}{r^2} \tag{10}$$

where θ is the angle between the incident atom trajectories and the normal to the condensing surface dA_c as seen in Figure 18.

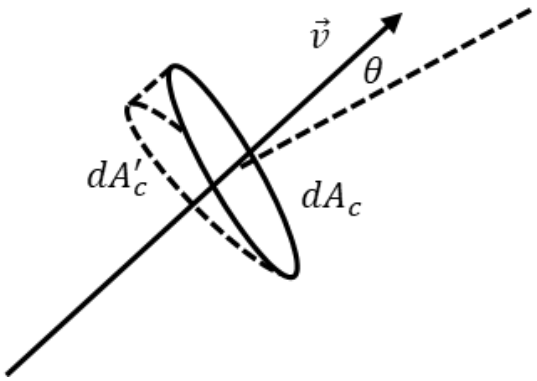

Figure 18. Atoms traveling at velocity $\vec{v}$ strike the condensing surface element dA_c. The same atoms that cross dA_c also cross its projected area dA_c', where $dA_e' = dA_c \cos\theta$. This shows the geometric relation used to evaluate the flux through the surface.

The total solid angle around a point is 4π. Therefore, the fraction of atoms emitted from dA_e that travel toward the surface element to dA_c is given by the ratio of the differential solid angle to the total solid angle:

$$\frac{d\omega}{4\pi} = \frac{dA_c \cos\theta}{4\pi r^2}. \tag{11}$$

Using this, the total number of molecules leaving the surface element and hitting the substrate element with velocity v can be expressed as

$$dN = \rho dV \frac{d\omega}{4\pi} f(v)dv, \tag{12}$$

where ρ is the number density of evaporant material, dV is the volume in which they reach the surface, and $f(v)dv$ is the velocity density, with speeds v and $v + dv$. This means ρdV is the number of atoms in dV, $d\omega/4\pi$ is the fraction that reach dA_c, and $f(v)dv$ is the number that have speeds between v and $v + dv$. Thus, Equation 12 becomes

$$dN = \rho v dt dA_e \cos\phi \frac{dA_c \cos\theta}{4\pi r^2} f(v)dv\,, \tag{13}$$

which can be rearranged to

$$\frac{d^4N}{dtdA_e dA_c dv} = \frac{\rho \cos\phi \cos\theta\, v}{4\pi r^2} f(v) \cdot \alpha, \tag{14}$$

where α was included to account for the fraction of evaporant atoms that actually cross the surface, as some atoms may move quickly but never exit the surface.

To find the function $f(v)$ the partition function can be used. For a molecule in the evaporant the energy for motion in one-dimension is

$$E = \frac{1}{2} m {v_x}^2, \tag{15}$$

so the one-dimensional single particle partition function is

$$Z_1 = \int_{-\infty}^{\infty} e^{\frac{-m{v_x}^2}{2kT}} dv_x = 2\int_0^{\infty} e^{\frac{-m{v_x}^2}{2kT}} dv_x. \tag{16}$$

Evaluating this integral gives

$$Z_1 = \frac{1}{2\left(\frac{m}{kT}\right)^{\frac{1}{2}}} \sqrt{\pi} = \sqrt{\frac{2\pi kT}{m}}, \tag{17}$$

where T is absolute temperature and m is the mass of a single atom. Using Equation 17, the partition function in three dimensions for a single particle is

$$Z = Z_1^3 = \left(\frac{2\pi kT}{m}\right)^{\frac{3}{2}}. \tag{18}$$

The probability function $P(v)$ can be found using the partition function as follows:

$$P(v)d^3v = \frac{e^{\frac{-mv^2}{2kT}} d^3v}{Z} = \frac{e^{\frac{-m({v_x}^2+{v_y}^2+{v_z}^2)}{2kT}}}{\left(\frac{2\pi kT}{m}\right)^{\frac{3}{2}}} d^3v. \tag{19}$$

This makes the probability between v and $v + dv$:

$$P(v)d^3v = P(v)dv_x dv_y dv_z\,, \tag{20}$$

which, after transforming to spherical velocity coordinates and integrating over solid angle, becomes

$$P(v)d^3v = P(v)4\pi v^2 dv. \tag{21}$$

Now, using Equation (19) gives:

$$f(v)dv = P(v)d^3v = \frac{e^{\frac{-mv^2}{2kT}}}{\left(\frac{2\pi kT}{m}\right)^{\frac{3}{2}}} 4\pi v^2 dv. \tag{22}$$

This means that Equation 14 becomes

$$\frac{d^3N}{dtdA_e dA_c} = \frac{\alpha\rho\cos\phi\cos\theta}{4\pi r^2} v \frac{e^{\frac{-mv^2}{2kT}}}{\left(\frac{2\pi kT}{m}\right)^{\frac{3}{2}}} 4\pi v^2 dv. \tag{24}$$

To include all atoms, integrate over all possible velocities, giving

$$\frac{d^3N}{dtdA_e dA_c} = \frac{\alpha\rho\cos\phi\cos\theta}{r^2} \int_0^\infty v^3 \frac{e^{\frac{-mv^2}{2kT}}}{\left(\frac{2\pi kT}{m}\right)^{\frac{3}{2}}} dv, \tag{25}$$

which becomes

$$\frac{d^3N}{dtdA_e dA_c} = \frac{\alpha\rho\cos\phi\cos\theta}{r^2} \left(\frac{m}{2\pi kT}\right)^{\frac{3}{2}} \left(\frac{1}{2\left(\frac{m}{2kT}\right)^2}\right). \tag{25}$$

This can be simplified to

$$\frac{d^3N}{dtdA_e dA_c} = \frac{\alpha\rho\cos\phi\cos\theta}{4\pi r^2} \sqrt{4\pi} \left(\frac{2kT}{m}\right)^{\frac{1}{2}}. \tag{26}$$

Now in order to convert from number/time to mass/time this must be multiplied by the mass of one molecule:

$$\frac{dM}{dt} = m\frac{dN}{dt} = \int_{A_e}\int_{A_c} \frac{m\alpha\rho\cos\phi\cos\theta}{4\pi r^2}\sqrt{4\pi}\left(\frac{2kT}{m}\right)^{\frac{1}{2}} dA_e dA_c\,. \tag{27}$$

Now, collecting constants into C this becomes

$$\frac{dM}{dt} = \int_{A_e}\int_{A_c} C\rho\,\frac{\cos\phi\cos\theta}{r^2}\,dA_e dA_c\,. \tag{28}$$

If both the evaporating and condensing surfaces are flat, parallel, and separated by a distance much larger than their horizontal dimensions, the geometric factors vary only weakly across the surfaces. By treating $\cos\phi$ and $\cos\theta$ as constants, Equation (28) becomes

$$\frac{dM}{dt} = C\rho\frac{\cos\phi\cos\theta}{r^2}A_e A_c\cdot\alpha. \tag{29}$$

This expression shows how the deposition rate depends both on the geometry and conditions of the system. dM/dt increases with the size of the evaporating area A_e and condensing area A_c, as well as with density ρ. The $\cos\phi$ and $\cos\theta$ components demonstrate the directional influence of evaporation and deposition, by showing that only the components of atomic flux normal to the surfaces contribute to the net deposition rate. At larger incidence angles, the projected flux onto the surface is reduced, leading to a smaller effective contribution. The inverse square dependence shows how deposition rate reflects the distance between the evaporator and substrate. The coefficient α represents the number of atoms that stick to the surface. This equation demonstrates the physical properties of vapor deposition, showing that proper conditions and alignments are required for the most yield.

However, this approximation does not strictly apply to the Houghton University lithium deposition chamber, where the source dimensions are not small compared to the source-to-substrate distance. In this case, $\cos\phi$, $\cos\theta$, and r vary significantly across the surfaces, and the full integral form of Equation (28) must be used to describe the deposition rate. A

numerical integration of Equation (28) has been performed in Ref [11]; the resulting mass distribution and comparison with experimental data are shown in Fig. 16 of that work.

Chapter 3

EXPERIMENTAL APPARATUS

3.1. Overview of the Lithium Deposition Chamber

3.1.1. The Purpose of this Evaporator

Chapter 1 introduced the need for a controlled lithium deposition system, and Chapter 2 developed the theoretical model describing how evaporated atoms travel and deposit onto a substrate. That analysis showed that factors such as vacuum level, system geometry, and alignment are significant factors in creating thin lithium depositions.

This chapter describes the lithium deposition chamber, shown in Figure 19, that was designed to incorporate those factors and build upon the success of the previous model . The system operates under vacuum conditions to enable ballistic transport of atoms from the evaporating surface to the substrate, minimizing collisions and ensuring predictable film growth. It consists of evaporating boats, a substrate holder positioned above the source, and instruments to control temperature and monitor chamber pressure.

The Houghton University lithium deposition chamber is used to produce thin lithium films on metal substrates. In operation, a DC power supply drives a current through a resistive evaporation boat, which heats the lithium source until evaporation occurs from its surface. By incorporating diode-based switching in the circuit, different evaporation boats can be selectively powered, allowing control over which source material is heated.

3.1.2. Exterior

The deposition chamber, as seen in Figure 19, is a 27 cm tall, 15 cm diameter stainless steel cylinder with five Conflat flange ports. The Conflat flange system allows for sealed connections between flanges, provided there is a fluorocarbon gasket “O-ring” inserted between them, corresponding to the flange size. The flanges are secured with bolts.

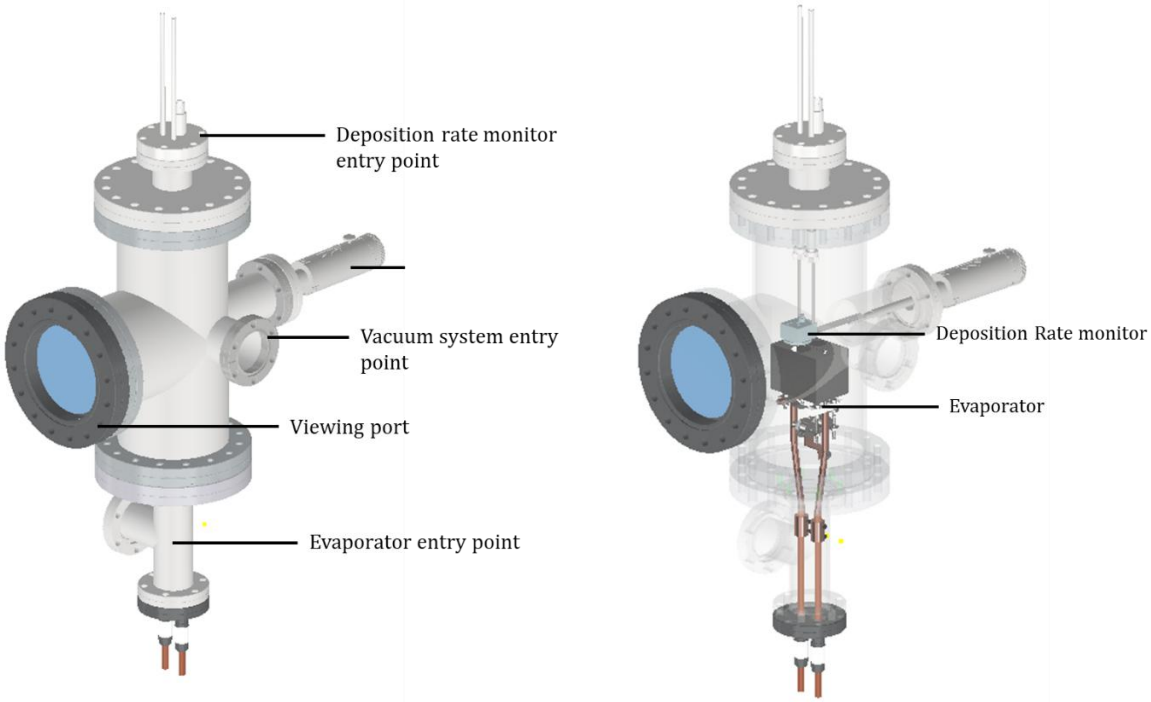

Figure 19. The new deposition system. The main chamber (Left) now has a viewing window, a linear motion feedthrough, and a rate monitor connected to it. The new evaporator is inserted from the bottom of the chamber. The main chamber will be connected to a vacuum system to evacuate the chamber for PVD. Also shown is the deposition system with a transparent main chamber (Right). The positioning of deposition rate monitor and the evaporator can now be seen.

The chamber has a DN100CF flange on both the top and bottom, with another DN100CF flange on the side, protruding 7 cm out. These provide a deposition rate monitor entry point, an evaporator entry point, and an observing window port, respectively. There are also two other flanges, both DN35CF, on the side of the main cylinder that provide a connection point for the vacuum system (to evacuate the deposition chamber) and a linear feedthrough (to manipulate the substrate used in PVD). They are positioned directly opposite the DN100CF side flange and 90 degrees from the side flange, as seen in Figure 19.

3.1.3. The Pumps

To evacuate the chamber, a vacuum system, as seen in Figure 20, is required. When the chamber is sealed, a Pascal 2005SD ALCATEL forepump is first used to remove the bulk of

the air, reducing the pressure to 10^{-3} Torr. Once this pressure is reached, a Veeco EP. 2A1 diffusion pump is engaged to further decrease the pressure to the range of 10^{-6} to 10^{-7} Torr.

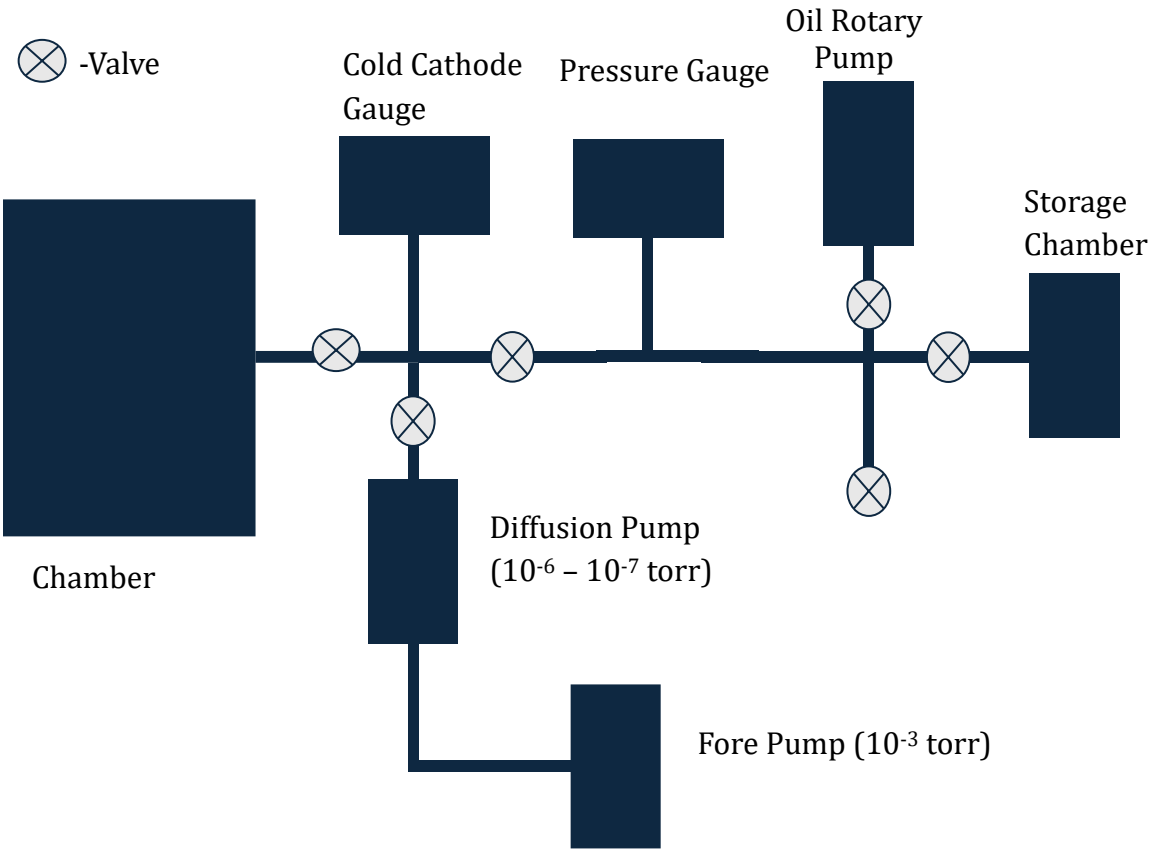

Figure 20. Schematic of the vacuum system used to evacuate the deposition chamber. The forepump and diffusion pump are connected to the main chamber through a series of valves, allowing staged pressure reduction and controlled isolation of different sections of the system.

These pumps are connected to one of the main chamber's DN35CF flanges via a system of valves, which allow increased control of pressure in the system. Closing valves allows the chamber to be vented then pumped down using a G-50D ULVAC oil rotary pump, all while the vacuum system stays pumped down by the diffusion pump and forepump. A storage chamber is also connected to the vacuum system, allowing lithium targets to be stored under vacuum to minimize oxidation and contamination.

3.1.4. Linear feedthrough

The second DN35CF flange will have a DN35CF to DN16CF adapter attached to it, so that a DN16CF linear feedthrough can be attached. The particular model to be used is a pneumatic MDC linear feedthrough, with a range of 75 mm.

This feedthrough, shown in Figure 21, will be attached to a substrate holder, meaning the stainless steel substrates used for Houghton's lithium targets can be manipulated whilst inside the chamber. This increased range of motion will allow the substrate to be oriented over top of either evaporating boat (allowing for multilayer targets to be created), as well as allowing the substrate to be moved out of the way so that evaporating molecules can instead travel to a deposition rate monitor.

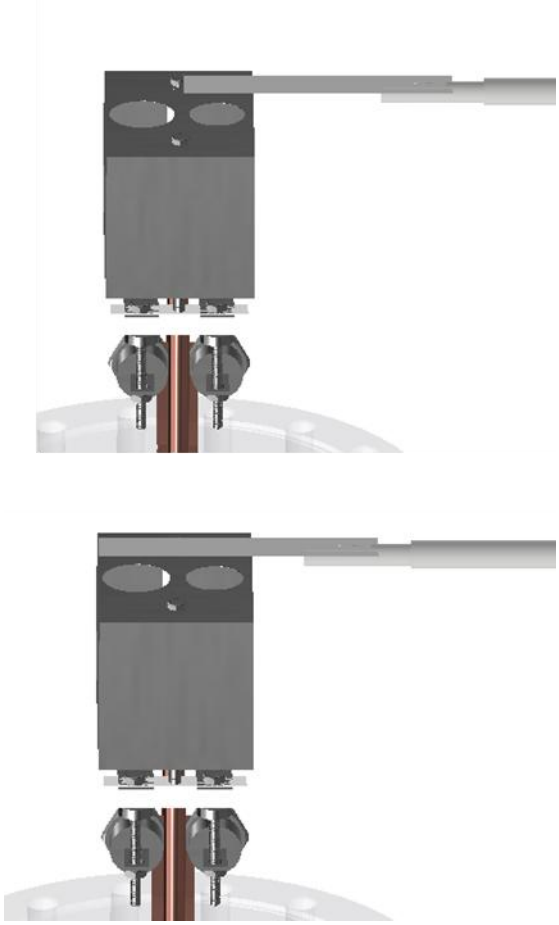

Figure 21. The linear feedthrough can move the substrate over either evaporating boat, allowing multilayer targets to be created.

3.1.5. Rate monitor

The top of the cylindrical deposition chamber will have a rotatable DN35CF to fixed DN100CF adapter attached. This will allow an INFICON model deposition rate monitor (with a DN35CF flange) to be inserted into the chamber. The monitor is a Quartz Crystal Microbalance monitor with an SL-B0E48 sensor head which will be inserted into the chamber. The sensor is supported by a set of tubes that both fix its position and provide a flow path for cooling water, preventing overheating during deposition. The feedthrough for this monitor allows data collected to be transferred out. The INFICON 21824 controller can be connected via USB to a computer. The program is called STM-2.

The adapting flange extends 4.5 cm and due to its rotatability the sensor can be oriented over one boat, then the flange can be loosened and rotated to orient the sensor over the other boat, as demonstrated in Figure 22. This allows the collection of data about both layers, if a multilayer target is being created.

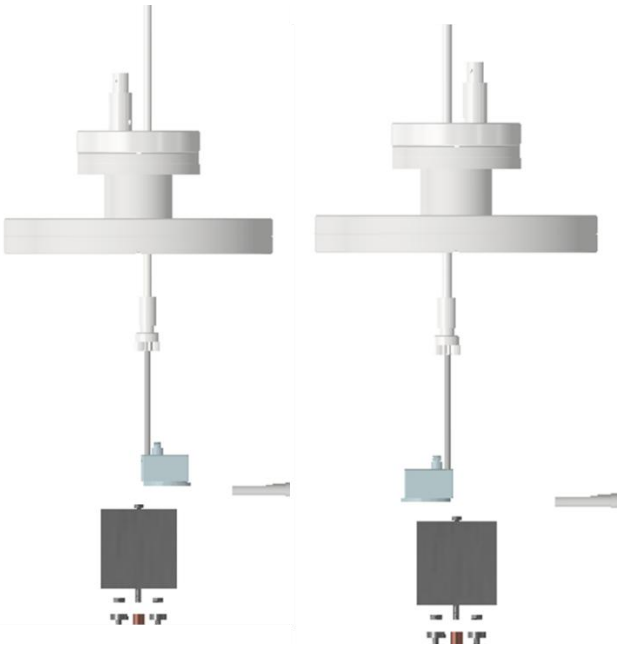

Figure 22. The rate monitor can be swiveled due to the rotatable adapter flange. This allows the sensing head to be oriented over either evaporating boat.

3.1.6. Evaporator connection

The bottom DN100CF flange of the chamber is to have a DN35CF to DN100CF fixed adapter attached. This will allow it to connect to a DN35CF tee. This will allow an electrical feedthrough for both the thermocouples and the evaporator to be attached.

A DN35CF thermocouple feedthrough is installed on the side port, allowing temperatures of the boats and the house to be measured during evaporation when the thermocouple is attached. The feedthrough is connected to a multimeter where temperatures can be read.

The vertical DN35CF flange will have the evaporator connected to it. It will have a Lesker electrical feedthrough attached, with 17 cm long, 0.63 cm diameter copper rods connected through. These copper rods provide a base for the evaporator, and allow current to travel into the chamber during evaporation. The copper rods are connected to a CircuitSpecialists CSI1560 DC power supply via two 4-conductor cables utilizing 2 AWG wire, which supply the required current.

The DN35CF tee allows both the evaporator and thermocouples to be installed and removed as a single assembly, simplifying setup and improving reliability by enabling thermocouples to be connected prior to insertion into the chamber.

3.1.7. Evaporator

The lithium deposition chamber evaporator exists to vaporize lithium for its deposition onto a substrate. It is constructed around a circuit with the purpose of heating up boats in which lithium and other materials can be placed. The circuit, shown in Figure 23, is designed in such a way that only one boat is heated at a time, depending on the orientation of the power source.

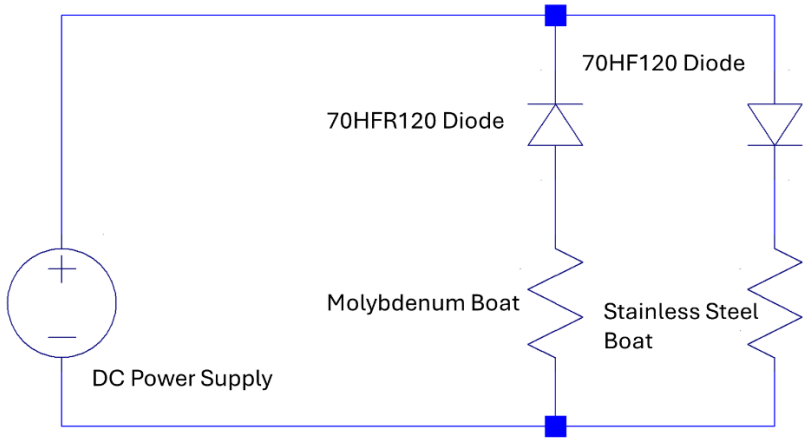

Figure 23. The evaporator circuit. When the power source is oriented as seen above, current flows through the rightmost branch, delivering current to the stainless steel boat. When the power source is inverted, current flows through the other branch, delivering current to the molybdenum boat. This ensures control over which boat is being heated. the right.

This circuit is realized in the evaporator assembly, shown in Figure 24. It mounts directly to the copper feedthrough described above. Shorter 12 cm bent copper rods, with diameter 0.63 cm, were attached to the feedthrough using 1.27 cm diameter machined copper barrels, with #8-40 thread 0.5 cm long set screws to maintain electrical contact between the bent rods and the feedthrough. The bend rods were bent twice, at an angle of 70 degrees, so that when they were attached to the feedthrough they ran parallel to one another, diverged, and then ran parallel again. The wider space between the bent rods allows the evaporation system to fit between.

In addition, the bent rods have a #6-32 threaded 3.8 cm long rod sticking out of the top, to support the stainless steel house. One of the threaded rods screws into a ceramic block with holes drilled 1 cm away from the threaded rod hole. The other threaded rod and bent rod connect to a 0.63 cm diameter horizontal copper rod with drilled holes 1 cm away from the larger hole, as pictured in Figure 25.

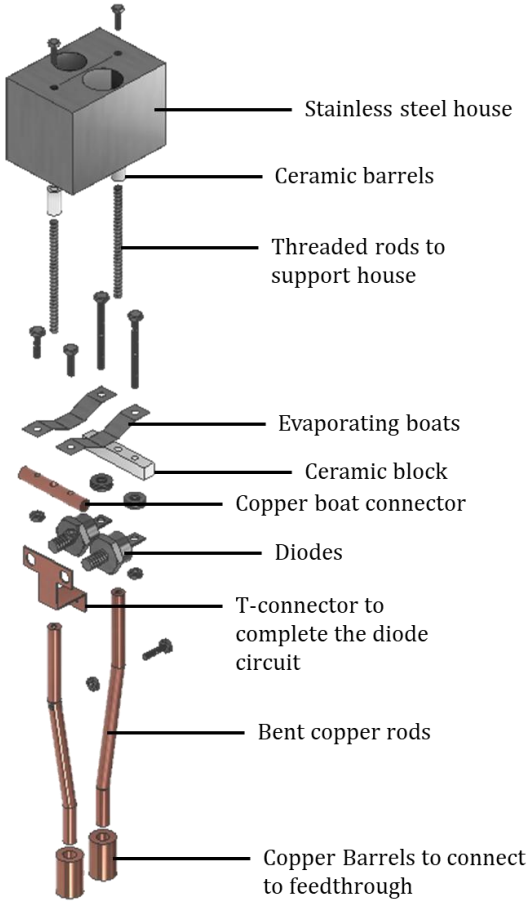

Figure 24. AutoCAD exploded view rendering of the evaporator. The barrels at the bottom secure the bent rods to a feedthrough (not pictured). The bent rods connect to long threaded rods and provide structure for the rest of the evaporator. The threaded rods secure both the horizontal copper rod and the ceramic block, and the house above. The copper rod and ceramic block are connected via two boats, and the ceramic block has thermal connection to a t-connector through two diodes.

The horizontal copper rod and ceramic block are parallel to one another and spaced so that the boats can connect to the drilled holes. The boats are different; one is a Lesker EVSME7005MO molybdenum electric boat, while the other is a lab-made stainless steel boat measuring 5 cm by 1 cm, fabricated from 0.0025 cm thick 304 stainless steel and dented using a 1.25 cm diameter ball bearing to create a divot. The copper rod has #6-36 threaded screws that connect the two boats on the other side, however the non-conducting ceramic

block has long #6-36 screws which secure both the boats and connect to diodes further down.

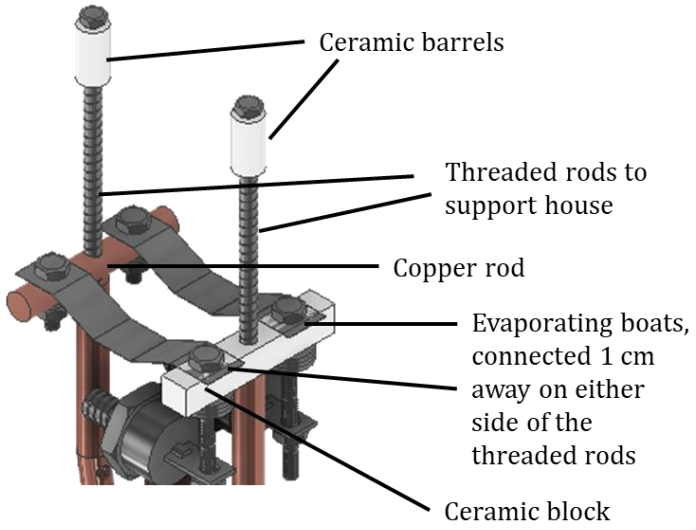

Figure 25. The copper rod and ceramic block, drilled and connected to the rest of the system. The stainless steel and molybdenum boats connect 1 cm away from the threaded rods that support the house.

The long screws on the ceramic connect to two different diodes, a 70HFR120 and a 70HF120. These diodes connect in the same way, but allow current to pass through oppositely. Their purpose is to pass current through only one boat at a time. These diodes are connected to a copper t-connector, which allows current to flow through whichever diode is facing the correct direction, as seen in Figure 26. The t-connector extends down a total of 1.65 cm and connects to the bent copper rod below the ceramic block with a #6-32 screw, completing the circuit.

The final part of the evaporator is the house. The long threaded rods from the bent copper rods extend past the horizontal copper rod and ceramic block and end with 1 cm long, 0.5 cm diameter ceramic barrels to prevent electrical contact. The barrels are screwed to a stainless steel house, cut with scissors out of 0.005 cm thick 321 stainless steel. The top of the house is 4 cm by 5.75 cm, and there is a 1.9 cm diameter hole cut with a drill press above the molybdenum boat and a 1.625 cm diameter hole cut with a drill press above the stainless steel boat. The house includes a divider, made from the same material, dividing the space

above the two boats. The house surrounds the boats, helping to confine the evaporated material and reduce unwanted deposition on surrounding components.

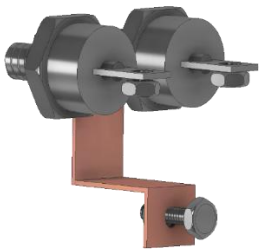

Figure 26. The t-connector with both the 70HFR120 and 70HF120 diodes connected. The bottom screw attaches the connector to the bent copper rod. This allows electrical connection from the bottom of the t-connector through whichever diode is facing the desired direction.

The new evaporator is mounted to the DN35CF tee at the bottom of the chamber, allowing it to be installed and removed more easily than the previous design . In this configuration, the O-ring that maintains the vacuum seal remains seated on the evaporator flange during insertion, preventing misalignment. The previous design required insertion through the side DN100CF port, where the O-ring was prone to displacement and could interfere with proper installation of the evaporator.

As explained, the new evaporator is connected to the DN35CF tee at the bottom of the chamber. This will allow the O-ring that maintains the vacuum seal during evacuation can rest on top of the evaporator flange as it is inserted into the chamber, making it easier to install. Previously the chamber was inserted into the DN100CF flange on the side of the chamber, so the O-ring often fell and interfered with the evaporator when installing.

Chapter 4

CONCLUSION

4.1. Status of the Chamber

While the system described in Chapter 3 has been drawn using the Autodesk Inventor CAD system, the chamber is not fully assembled. The house still needs to be cut out of stainless steel, and a lithium boat needs to be made. However the rest of the evaporator can be assembled as seen in Figure 27. The deposition chamber still has the previous iteration of the evaporator inside of it, as the new one has not yet been built.

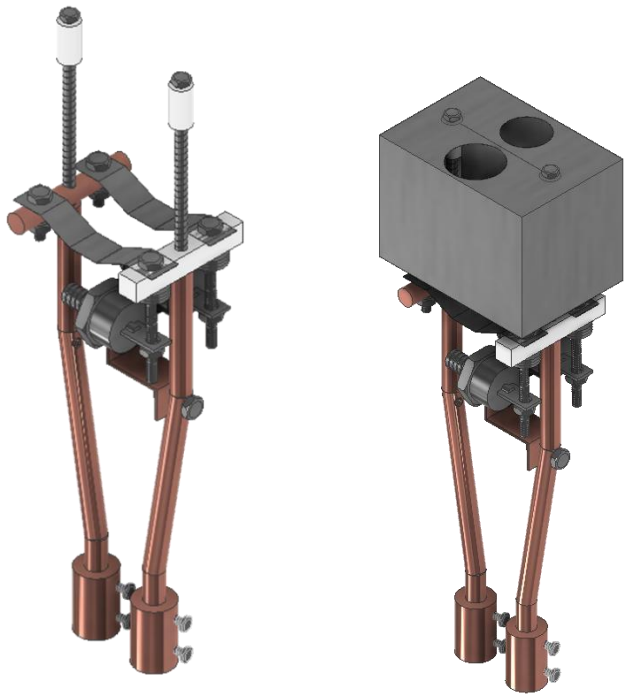

Figure 27. Rendering of the new evaporator, fully assembled. This will attach to a conducting feedthrough and will be used to make lithium depositions.

Once completed, the new evaporator will allow improved control of the deposition process through simplified installation, selective heating of boats, and the ability to produce multilayer films. The incorporation of a divider between the boats prevents cross-contamination of materials during evaporation. Also, the redesigned structure avoids the use of fragile ceramic screws that were used in the current evaporator, increasing structural reliability. A viewport on the side of the chamber allows for better monitoring of the PVD process. Together, these features will improve the purity and precision of Hoghton's lithium film fabrication.

4.2. Future Plans

The main focus of this project was constructing a new evaporator, however there are other critical aspects of the project as well. A linear feedthrough was aquired, but it must be modified before it is installed. Although the feedthrough is designed for pneumatic actuation, it will be operated in a fixed, manual configuration by incorporating a set screw to lock the external shaft in place. This modification will allow the feedthrough to maintain a stable substrate position during deposition.

The linear feedthrough provides increased control over the PVD process by allowing the substrate position to be adjusted during deposition. By extending or retracting the feedthrough, the substrate can be aligned over either evaporation boat, enabling sequential deposition and the fabrication of multilayer targets. Additionally, the substrate holder includes an opening that allows it to be moved out of the deposition path, so that evaporated atoms pass through to the rate monitor instead of depositing on the substrate. This capability enables in situ measurement of deposition rate while maintaining flexibility in substrate positioning.

Additionally, a new argon glove bag should be developed. A larger glove bag will allow the use of a very long feedthrough for making films that can be inserted into the SUNY Geneseo pelletron target chamber without being exposed to air.

In the future it is hoped that isotopically pure ^{6}Li and ^{7}Li films can be made, as these are valuable for nuclear physics research. Lithium naturally occurs as a mixture of the isotopes

^{6}Li and ^{7}Li, which are both stable forms of lithium with differing neutron counts. Natural lithium is the naturally occurring mixture of the two isotopes, where approximately 7.5% is ^{6}Li and 92.5% is ^{7}Li. Using isotopically pure samples removes the contribution of the naturally occurring isotope mixture, allowing for more controlled nuclear interactions, since the nuclear behavior is different between isotopes. This improved control enables more accurate and interpretable measurements of reaction rates in TNSA and ICF experiments, where small variations in isotopic composition significantly affect the observed nuclear reactions.

References

[1] M. Yuly, S. Padalino, N. Harley, A. Hotchkiss, C. Lei, and A. Martin, "A new technique for measuring light ion nuclear reactions using TNSA," in Nuclear and Plasma Diagnostics for the EP-OMEGA and MTW Laser Systems, LLE Proposal for Subaward 416231-G, 2023 (unpublished).

[2] M. Yuly, S. Padalino, A. Brown, A. Hotchkiss, C. Lei, and A. Martin, "Trapping and detecting trace radioactive isotopes produced in ICF implosions," in Nuclear and Plasma Diagnostics for the EP-OMEGA and MTW Laser Systems, LLE Proposal for Subaward 416231-G, 2022 (unpublished).

[3] M. Yuly, A. Bo, A. Belanger, O. Fall, S. Padalino, C. Freeman, "Nuclear Physics Using Ultrafast High-Power Laser Ion Acceleration," in Nuclear and Plasma Diagnostics for the EP-OMEGA and MTW Laser Systems, LLE Proposal for Subaward 416231-G, 2024 (unpublished).

[4] M. Yuly, A. Bo, S. Plymale, D. Vara, C. Freeman, G. Marcus, S. Padalino, "A Phoswich Detector System for Nuclear Measurements Using ICF and TNSA," in Nuclear and Plasma Diagnostics for the EP-OMEGA and MTW Laser Systems, LLE Proposal for Subaward 416231-G, 2025 (unpublished).

[5] I. Langmuir, *Phys. Rev.* **34**, 401 (1929).

[6] R. von Pohl and P. Pringsheim, *Verh. Dtsch. Phys. Ges.* **14**, 506 (1912).

[7] R. Boyle, *New Experiments Physico-Mechanical, Touching the Spring of the Air and Its Effects* (H. Hall, Oxford, 1660).

[8] W. Crookes, *Proc. R. Soc. London* **30**, 469 (1879).

[9] J. C. Maxwell, *Philos. Trans. R. Soc. London* **170**, 231 (1879)

[10] J. H. Singleton, *J. Vac. Sci. Technol. A* **2**, 126 (1984).

[11] C. Lei, B.S. thesis, (Houghton University, 2024).

[12] D. M. Mattox, *Handbook of Physical Vapor Deposition (PVD) Processing* (Noyes Publications, Westwood, NJ, 1998).

[13] R. B. Darling, EE-527 Microfabrication Lecture Notes, California Institute of Technology (unpublished).